Earth and Planetary Science Letters 528 (2019) 115850

Contents lists available at ScienceDirect

Earth and Planetary Science Letters

www.elsevier.com/locate/epsl

An essential role for sulfur in sulfide-silicate melt partitioning of gold and magmatic gold transport at subduction settings

Yuan Li [a,b,*], Lu Feng [a], Ekaterina S. Kiseeva [c,d], Zenghao Gao [a], Haihao Guo [b], Zhixue Du [a], Fangyue Wang [e], Lanlan Shi [a]

[a] State Key Laboratory of Isotope Geochemistry, Guangzhou Institute of Geochemistry, Chinese Academy of Sciences, Guangzhou 510640, China
[b] Bayerisches Geoinstitut, Universität Bayreuth, 95440 Bayreuth, Germany
[c] Department of Earth Sciences, University of Oxford, Oxford OX1 3AN, UK
[d] School of Biological, Earth and Environmental Sciences, University College Cork, Cork, Ireland
[e] School of Resources and Environmental Engineering, Hefei University of Technology, Hefei 230009, China

ARTICLE INFO

Article history:
Received 26 June 2019
Received in revised form 17 September 2019
Accepted 18 September 2019
Available online 2 October 2019
Editor: F. Moynier

Keywords:
gold
sulfur
sulfide
silicate melt
partition coefficient
subduction zone

ABSTRACT

Sulfide-silicate melt partitioning controls the behavior of gold in magmas, which is critical for understanding the Earth's deep gold cycle and formation of gold deposits. However, the mechanisms that control the sulfide-silicate melt partitioning of gold remain largely unknown. Here we present constraints from laboratory experiments on the partition coefficient of gold between monosulfide-solid-solution (MSS) and silicate melt ($D_{Au}^{MSS/SM}$) under conditions relevant for magmatism at subduction settings. Thirty-five experiments were performed in Au capsules to determine $D_{Au}^{MSS/SM}$ at 950-1050 °C, 0.5-3 GPa, oxygen fugacity (fO_2) of ~FMQ-1.7 to FMQ+2.7 (FMQ refers to the fayalite-magnetite-quartz buffer), and sulfur fugacity (fS_2) of −2.2 to 2.1, using a piston cylinder apparatus. The silicate melt composition changes from dry to hydrous andesite to rhyolite. The results obtained from electron microprobe and laser-ablation ICP-MS analyses show that the gold solubility in silicate melts ranges from 0.01 to 55.3 ppm and is strongly correlated with the melt sulfur content $[S]_{melt}$ at fO_2 of ~FMQ-1.7 to FMQ+1.6, which can be explained by the formation of complex Au-S species in the silicate melts. The gold solubility in MSS ranges from 130 to 2800 ppm, which is mainly controlled by fS_2. $D_{Au}^{MSS/SM}$ ranges from 10 to 14000 at fO_2 of ~FMQ-1.7 to FMQ+1.6, the large variation of which can be fully explained by combined $[S]_{melt}$ and fS_2. Therefore, all of the parameters that can directly affect $[S]_{melt}$ and fS_2, such as alkali metals, water, FeO, and fO_2, can indirectly affect $D_{Au}^{MSS/SM}$. The mechanisms that control the sulfide-silicate melt partitioning of gold and the other chalcophile elements, such as Ni, Re, and Mo, differ significantly. This is because gold is dissolved mainly as Au-S species in the silicate melts, while the other chalcophile elements are dissolved mainly as metal oxides in the silicate melts. Applying the correlation between $D_{Au}^{MSS/SM}$ and $[S]_{melt}$ to slab melting and arc magmatic differentiation under different redox conditions, we find that ancient to modern slab melts carry negligible to less than 25% of the slab gold to the subarc mantle; however, gold-enrichment can occur in MSS-saturated arc magmas that have differentiated under moderately oxidized conditions with fO_2 between FMQ and FMQ+1.6, in particular if the magmatic crystallization follows a fractional crystallization model. We conclude that moderately oxidized magmas with high contents of alkali metals, sulfur, and water, owing to their low $D_{Au}^{MSS/SM}$ and efficient magma-to-fluid transfer of gold and sulfur, have a high potential to form gold deposits.

1. Introduction

Understanding the factors that control the behavior of gold (Au) in magmas is of fundamental importance in understanding magmatic Au transport, Au mineralization, and the exploration of Au deposits in Earth's crust (Botcharnikov et al., 2011; Jégo et al., 2010; Muntean et al., 2011; Tassara et al., 2017; Zajacz et al., 2013; Zajacz et al., 2010). The behavior of Au as a chalcophile element is controlled by sulfides, and Au-rich magmas form readily when sulfides are absent during magmatic genesis and/or differentiation (Mungall, 2002; Sillitoe, 1997). However, sulfides are

* Corresponding author.
E-mail address: Yuan.Li@gig.ac.cn (Y. Li).

https://doi.org/10.1016/j.epsl.2019.115850

ubiquitous in mantle rocks (Alard et al., 2011), subduction zone rocks (Aulbach et al., 2012; Evans et al., 2014), and arc magmatic rocks (Lee et al., 2012; Parat et al., 2011; Wallace and Edmonds, 2011). Depending on the temperature, pressure, and composition, these sulfides can be crystalline monosulfide-solid-solution (MSS) and/or sulfide liquid (Bockrath et al., 2004; Jenner, 2017; Li and Audétat, 2012). Recent studies have demonstrated that the main sulfide phase fractionated during arc magmatic differentiation is MSS, which causes the depletion of Cu in variously evolved arc magmas and the continental crust (Jenner, 2017; Lee et al., 2012; Li and Audétat, 2013; Wang et al., 2018). The enrichment of Au in magmas is a key ingredient in the production of giant Au deposits and districts (Mungall, 2002; Muntean et al., 2011; Sillitoe, 1997; Tassara et al., 2017), so it is of great interest to investigate whether Au-enrichment can form in the differentiating arc magmas that are saturated with MSS. On the other hand, geochemical studies and experimental simulations suggest that the subducting slab contributes sulfur via slab melts or fluids to the subarc mantle (Jégo and Dasgupta, 2013, 2014; Wallace, 2005), although most of the sulfur in the subducting slab enters the deep mantle (Evans, 2012; Jégo and Dasgupta, 2013). However, the capability of such S-bearing slab melts or fluids in transporting slab chalcophile elements, in general, and Au, in particular, to the subarc mantle has received little attention (Canil and Fellows, 2017). The fate of Au during slab melting is essentially linked to the long-term deep Au cycle, as extensive melting of altered oceanic crust and/or sediments occurs in both ancient and modern subduction zones (Martin and Moyen, 2002; Spencer et al., 2017).

Investigating the behavior of Au in sulfide-saturated magmas requires knowledge of the sulfide-silicate melt partitioning for Au. Most recent studies show that the sulfide liquid-silicate melt partition coefficient of Au ($D_{Au}^{SL/SM}$) varies from ~1000 to 30000 under conditions of 1000-1250 °C, 1 bar to 2.5 GPa, and fO_2 of FMQ-3 to FMQ+1 (Botcharnikov et al., 2013; Li and Audétat, 2013). Whereas, the MSS-silicate melt partition coefficient of Au ($D_{Au}^{MSS/SM}$) is lower, varying from ~40 to 3000 under conditions of 800-1250 °C, 1 bar to 2.5 GPa, and fO_2 of FMQ-3 to FMQ+1 (Botcharnikov et al., 2011; Li and Audétat, 2013, 2015; Zajacz et al., 2013). Assuming a typical chalcophile element M dissolves in the silicate melt as metal oxides (Kiseeva and Wood, 2013, 2015), the sulfide-silicate melt partitioning of the element M can be described as:

$$\log D_M^{Sulf/SM} = A + \frac{x}{2}\log[FeO] \quad (1)$$

in which A is a constant; x is a constant related to valence state of the element M; and [FeO] is the FeO content in the silicate melt in wt.%. In case the valence state of the element M varies with fO_2, $\log D_M^{Sulf/SM}$ can be described by including an fO_2-term in Eq. (1) (Feng and Li, 2019; Li and Audétat, 2015):

$$\log D_M^{Sulf/SM} = A + B\Delta FMQ + \frac{x}{2}\log[FeO] \quad (2)$$

in which B is a coefficient for ΔFMQ, and ΔFMQ refers to fO_2 relative to the FMQ (fayalite-magnetite-quartz) buffer. The relationships between $D_M^{Sulf/SM}$, the melt FeO content, and fO_2, as summarized by Eqs. (1) and (2), have been successfully tested on a large number (>15) of chalcophile elements and have proved to be valid for a broad range of temperatures and sulfide and silicate melt compositions (Feng and Li, 2019; Kiseeva and Wood, 2013, 2015; Li and Audétat, 2015). However, as shown in Fig. S1, the models of Eqs. (1) and (2) are not followed by Au, although Li and Audétat (2015) and Zajacz et al. (2013) observed an increase from 6000 to 30000 for $D_{Au}^{SL/SM}$ and 180 to 2900 for $D_{Au}^{MSS/SM}$, respectively, when the silicate melt varies from basalt to rhyolite at fixed fO_2. Fitting all of the $D_{Au}^{MSS/SM}$ data compiled in Fig. S1 into Eqs. (1) and (2) yielded R^2 of 0.16 and 0.11, respectively, which suggests that neither the model of Eq. (1) nor (2) can interpret the MSS-silicate melt partitioning of Au. Therefore, the mechanism that controls the sulfide-silicate melt partitioning of Au and the other chalcophile elements could differ significantly.

The solubility of Au in S-free silicate melts, dissolved mainly as Au^+ oxide, is rather low (<1 ppm) under mantle-crust conditions (Botcharnikov et al., 2011; Jégo and Pichavant, 2012; Jégo et al., 2010; Li and Audétat, 2013; Zajacz et al., 2013). Several recent studies, however, show the enhancement of Au solubility by sulfide (S^{2-}) via the formation of Au-sulfide species in the silicate melts at 800-1200 °C and 0.2-1.5 GPa (Botcharnikov et al., 2011; Jégo et al., 2016; Jégo and Pichavant, 2012; Jégo et al., 2010; Li and Audétat, 2013; Zajacz et al., 2013; Zajacz et al., 2012). The sulfur in the silicate melts may thus play an important role in controlling the sulfide-silicate melt partitioning of Au. However, the actual role played by sulfur and the role played by other parameters that potentially affect $D_{Au}^{SL/SM}$ or $D_{Au}^{MSS/SM}$ have never been investigated. In this study, we investigate systematically the MSS-silicate melt partitioning of Au by measuring the solubility of Au in coexisting MSS and silicate melt under conditions relevant for slab melting and arc magmatic differentiation. We find that $D_{Au}^{MSS/SM}$ varies by more than three orders of magnitudes and the variation is strongly controlled by sulfur fugacity (fS_2) and the melt sulfur content over an fO_2 range of ~FMQ-1.7 to FMQ+1.6. These new findings place tight constraints on the deep Au cycle and the potential of arc magmas in forming Au deposits at subduction settings.

2. Experimental methods

2.1. Starting materials

The starting materials included synthetic and natural silicate glasses and rocks, synthetic Ni-Cu-bearing sulfide, natural magnetite, distilled water, reagent-grade $CaSO_4$ (anhydrite), FeS (pyrrhotite) and graphite powder. The dacitic glass was synthesized from analytical grade oxides (MgO, FeO, MnO, NiO, SiO_2, TiO_2, Al_2O_3, Cr_2O_3, and P_2O_5) and carbonates (Na_2CO_3, K_2CO_3, and $CaCO_3$). The natural silicate rocks included partly glassy andesite and glassy rhyolite. The major element compositions of all of the used silicate glasses/rocks are given in Table S1. The Ni-Cu-bearing sulfide was synthesized at 1200 °C in an evacuated SiO_2 glass ampoule using the method described in Li and Audétat (2012); its major element composition is given in Table S1. All of the starting silicates and sulfides were powdered to ensure homogeneity before loading into sample capsules.

2.2. Sample capsules and high-pressure experiments

Thirty-five experiments were performed to study the partitioning of Au in sulfide ± sulfate and silicate melt systems under conditions relevant for slab melting and arc magmatic differentiation (Table 1). A first set of four experiments was performed at 950-1040 °C and 1-3 GPa, with andesitic silicate and ~15 wt.% Cu-Ni-bearing sulfide contained in Au capsules. In each Au capsule, ~5 wt.% distilled water was added to generate hydrous silicate melt. For this set of experiments, the fO_2 was not buffered by any fO_2 buffer, and the run duration ranged from 48 to 312 hours.

A second set of thirteen experiments was performed at 1040 °C and 0.5-3 GPa, with dacitic silicate and ~15 wt.% Cu-Ni-bearing sulfide or FeS (pyrrhotite) contained in Au capsules. In each Au capsule, ~0-10 wt.% distilled water was added. In addition, ~2-15 wt.% anhydrite was added in the Au capsules of runs Sulf-3, Sulf-5, Da-2A, and Da-1B to obtain a high fO_2. Available studies show that the fO_2 for the coexistence of sulfide and anhydrite in natural

Table 1
Overview of experimental conditions and run products.

Run No.	T (°C)	P (GPa)	Duration (h)	Capsule	Starting material	Main run products	S^{6+}/S_{tot}	[a] $\log fO_2$ (ΔFMQ)	[b] $\log fS_2$	S in SM (ppm)	Au in SM (ppm)	Au in MSS (ppm)	$D_{Au}^{MSS/SM}$	Melt NBO/T
Set-1 Experiments														
A-1	950	2	96	Au	Ande+Sulf+H_2O	MSS+SM+Cpx+Grt	−0.05 ± 0.00	n.d.	−0.39	401 ± 167	0.4 ± 0.1	134 ± 8	386 ± 160	0.093
A-2	950	1	192	Au	Ande+Sulf+H_2O	MSS+SM+Cpx+Mag	0.60 ± 0.25	1.47 ± 0.47	1.11	976 ± 88	1.6 ± 0.6	697 ± 46	436 ± 166	0.088
A-4	975	3	312	Au	Ande+Sulf+H_2O	MSS+SM+Cpx+Grt	n.d.	n.d.	0.86	248 ± 45	0.3 ± 0.0	359 ± 68	1237 ± 300	0.044
A-6	1040	2	48	Au	Ande+Sulf+H_2O	MSS+SM+Cpx+Grt+Mag	n.d.	n.d.	1.18	1040 ± 267	1.5 ± 0.1	453 ± 30	309 ± 31	0.225
Set-2 Experiments														
Sulf-1	1040	0.6	144	Au	Daci+Sulf+H_2O	MSS+SM+Mag	0.68 ± 0.22	1.63 ± 0.42	0.48	1182 ± 169	11.0 ± 0.4	888 ± 120	81 ± 11	0.196
Sulf-2	1040	0.6	168	Au	Daci+Sulf+H_2O	MSS+SM	0.53 ± 0.28	1.34 ± 0.56	0.92	659 ± 84	4.7 ± 0.5	750 ± 82	160 ± 24	0.175
Sulf-3	1040	0.6	144	Au	Daci+Sulf+H_2O +Anhy	MSS+SM+Mag	0.56 ± 0.21	1.39 ± 0.39	0.92	1121 ± 124	5.2 ± 1.0	801 ± 215	154 ± 51	0.111
Sulf-4	1040	2.0	168	Au	Daci+Sulf+H_2O	MSS+SM+Cpx+Grt	n.d.	n.d.	0.48	243 ± 21	0.2 ± 0.1	459 ± 42	2691 ± 885	0.087
Sulf-6	1040	3.0	96	Au	Daci+Sulf+H_2O	MSS+SM+Cpx+Grt	0.52 ± 0.27	1.32 ± 0.54	2.08	637 ± 21	1.0 ± 0.3	1083 ± 94	1081 ± 334	0.076
Da-2B	1040	2	48	Au	Daci+FeS+H_2O	MSS+SM+Cpx+Grt	0.32 ± 0.06	0.94 ± 0.13	1.18	358 ± 45	0.63 ± 0.03	1599 ± 125	2531 ± 222	0.125
Da-1C	1040	0.5	48	Au	Daci+FeS	MSS+SM+Cpx	n.d.	n.d.	0.06	148 ± 40	0.19 ± 0.08	482 ± 114	2503 ± 1230	0.082
Da-1A	1040	0.5	48	Au	Daci+FeS+Graph	MSS+SM+Graph+Cpx	n.d.	−1.67	0.12	165 ± 76	0.44 ± 0.25	911 ± 84	2069 ± 1207	0.075
Da-3A	1040	0.5	35	Au	Daci+FeS+H_2O	MSS+SM+Cpx	0.56 ± 0.11	1.39 ± 0.39	−1.07	550 ± 141	cont.	556 ± 19	n.d.	0.212
Da-3B	1040	0.5	35	Au	Daci+FeS+Graph+H_2O	MSS+SM+Graph+Cpx	n.d.	−1.67	−0.87	196 ± 88	cont.	226 ± 47	n.d.	0.199
Sulf-5	1040	2.0	120	Au	Daci+Sulf+H_2O +Anhy	MSS+SM+Cpx+Anhy	0.75 ± 0.10	1.79 ± 0.22	1.82	1674 ± 76	2.0 ± 0.7	1422 ± 149	722 ± 252	0.165
Da-2A	1040	2	48	Au	Daci+FeS+Anhy+H_2O	MSS+SM+Cpx+Anhy	0.96 ± 0.04	2.74 ± 0.34	1.48	5536 ± 376	2.73 ± 0.08	2181 ± 534	799 ± 197	0.273
Da-1B	1040	0.5	48	Au	Daci+FeS+Anhy	MSS+SM+Anhy	0.75 ± 0.00	1.79 ± 0.00	1.27	1824 ± 126	3.28 ± 0.40	528 ± 177	161 ± 58	0.221
Da-1D	1040	0.5	48	Au	Daci+Anhy	SM+Anhy+Mag	0.84 ± 0.21	2.04 ± 0.51	n.d.	1032 ± 55	0.34 ± 0.05	n.d.	n.d.	0.135
Set-3 Experiments														
Rh-3A	1040	2	48	Au	Rhyo+FeS+H_2O	MSS+SM	0.33 ± 0.13	0.96 ± 0.31	1.34	316 ± 57	0.49 ± 0.03	1886 ± 47	3820 ± 259	0.072
Rh-1C	1040	0.5	48	Au	Rhyo+FeS	MSS+SM	n.d.	n.d.	0.54	90 ± 30	0.055	378 ± 80	6873 ± 1455	0.064
Rh-1D	1040	0.5	48	Au	Rhyo+FeS+Graph	MSS+SM+Graph	n.d.	−1.67	−0.57	50 ± 10	0.012 ± 0.005	175 ± 20	14194 ± 1622	0.056
Rh-2C	1000	0.5	48	Au	Rhyo+FeS+Graph	MSS+SM+Graph	n.d.	−1.67	0.18	144 ± 72	0.12 ± 0.08	n.d.	n.d.	0.054
Rh-4B	1040	0.5	35	Au	Rhyo+FeS+H_2O	MSS+SM	n.d.	n.d.	−0.87	63 ± 36	0.05 ± 0.02	393 ± 100	8363 ± 3412	0.012
Rh-4A	1040	0.5	35	Au	Rhyo+FeS+Graph+H_2O	MSS+SM+Graph	n.d.	−1.67	−0.75	67 ± 46	0.05 ± 0.02	253 ± 22	5554 ± 3000	0.014
Rh-1B	1040	0.5	48	Au	Rhyo+FeS+Anhy	MSS+SM+Anhy	0.61 ± 0.23	1.49 ± 0.43	1.08	792 ± 130	2.86 ± 0.24	2090 ± 248	730 ± 106	0.129
Rh-2A	1000	0.5	48	Au	Rhyo+FeS+Anhy	MSS+SM+Anhy	0.63 ± 0.17	1.53 ± 0.32	1.19	280 ± 32	0.79 ± 0.04	1459 ± 271	1856 ± 355	0.039
Rh-3B	1040	2	48	Au	Rhyo+FeS+Anhy+H_2O	MSS+SM+Anhy	0.80 ± 0.05	1.92 ± 0.13	1.61	5107 ± 506	2.74 ± 0.07	2777 ± 282	1015 ± 107	0.140
Rh-1A	1040	0.5	48	Au	Rhyo+Anhy	SM+Anhy	n.d.	n.d.	n.d.	63 ± 15	0.10 ± 0.03	n.d.	n.d.	0.015
Rh-2B	1000	0.5	48	Au	Rhyo+Anhy	SM+Anhy	n.d.	n.d.	n.d.	48 ± 29	cont.	n.d.	n.d.	0.012
Set-4 Experiments														
C-9a	1000	0.5	45	Au	Daci+Sulf+H_2O+Mag+$Au_{95}Cu_{05}$	MSS+SM	0.34 ± 0.29	0.98 ± 0.60	−2.17	693 ± 52	3.1 ± 0.2	220 ± 24	70 ± 9	0.302
C-9b	1000	0.5	45	Au	Rhyo+Sulf+H_2O+Mag+$Au_{95}Cu_{05}$	MSS+SM	0.47 ± 0.22	1.23 ± 0.45	−1.28	827 ± 21	3.2 ± 0.3	280 ± 19	89 ± 11	0.294
C-10a	1000	0.5	43	Au	Daci+Sulf+H_2O+Mag+Anhy+$Au_{95}Cu_{05}$	MSS+SM	0.50 ± 0.17	1.28 ± 0.32	−1.05	1511 ± 113	13.4 ± 0.3	370 ± 30	28 ± 2	0.375
C-10b	1000	0.5	43	Au	Rhyo+Sulf+H_2O+Mag+Anhy+$Au_{95}Cu_{05}$	MSS+SM	0.20 ± 0.04	0.65 ± 0.12	−1.06	704 ± 65	3.5 ± 0.5	670 ± 61	180 ± 23	0.288
C-13a	1000	0.5	46	Au	Daci+Sulf+H_2O+Anhy+$Au_{95}Cu_{05}$	MSS+SM	0.30 ± 0.21	0.90 ± 0.67	n.d.	3180 ± 677	55.3 ± 2.2	570 ± 190	10 ± 3	0.441
C-13b	1000	0.5	46	Au	Rhyo+Sulf+H_2O+Anhy+$Au_{95}Cu_{05}$	MSS+SM	0.21 ± 0.05	0.68 ± 0.15	n.d.	1754 ± 114	8.1 ± 1.8	350 ± 50	43 ± 12	0.323

Ande=andesite; Daci=dacite; Rhyo=rhyolite; Mag=magnetite; Anhy=anhydrite; MSS=crystalline monosulfide solid solution; SM=quenched silicate melt.
a. See the Supplementary Materials for the estimation of oxygen fugacity. b. 1-σ deviation for the estimated $\log fS_2$ is below 0.1 based on the replicate analyses of MSS.
n.d. not determined; cont. contaminated by Au nuggets so the data are discarded.
NBO/T=2 Total O/T-4 (T=Si+Ti+Al+Cr+P).

andesitic to rhyolitic arc magmas is usually higher than FMQ+1.5 (Chang and Audétat, 2018; Parat et al., 2011). Therefore, the addition of ~2-15 wt.% anhydrite in runs Sulf-3, Sulf-5, Da-2A, and Da-1B could enable us to obtain a relatively high fO_2 that is associated with oxidized arc magmas. Approximately 10 wt.% graphite powder was added at the bottom of each Au capsule of runs Da-1A and Da-3B. At graphite-saturation, the experimental fO_2 must be no larger than the C-CO_2 buffer (~1-2 log units below FMQ). Therefore, runs Da-1A and Da-3B should reach a rather low fO_2. In run Da-1D, only anhydrite but no sulfide was added in the Au capsule. For other runs (Sulf-1, Sulf-2, Sulf-4, Sulf-6, Da-2B, Da-1C, and Da-3A), the fO_2 was not constrained by any fO_2 buffer. The run duration of this set of fourteen experiments ranged from 96 to 168 hours.

A third set of eleven experiments was performed at 1000-1040 °C and 0.5-2 GPa, with rhyolitic silicate, ~0-10 wt.% distilled water, and ~20 wt.% FeS (pyrrhotite) and/or anhydrite contained in Au capsules. In runs Rh-1B, Rh-2A, and Rh-3B, both FeS and anhydrite were added to the Au capsules; whereas in runs Rh-1A and Rh-2B, only anhydrite but no sulfide was added to the Au capsules. In runs Rh-1D, Rh-2C, and Rh-4A, ~10 wt.% graphite powder was added at the bottom of each Au capsule, to obtain a low fO_2. The run duration of this set of experiments ranged from 35 to 48 hours.

A fourth set of six experiments was performed at 1000 °C and 0.5 GPa in Au capsules (runs C-9a, C-9b, C-10a, C-10b, C-13a, and C-13b). The major and trace element compositions of this set of experiments have been reported in our previous study (Li and Audétat, 2015), but S^{6+}/S_{tot} in the silicate melts was not measured and the SCSS and $D_{Au}^{MSS/SM}$ data were not discussed. In the Set-4 experiments, the starting materials included ~84-87 wt.% dacitic or rhyolitic silicate, ~10 wt.% Cu-Ni-bearing sulfide, and ~0-6 wt.% distilled water. In addition, ~10 wt.% magnetite was added to each Au capsule of runs C-9a, C-9b, C-10a, and C-10b, and ~3 wt.% anhydrite was added to each Au capsule of runs C-10a, C-10b, C-13a, and C-13b (Table 1). The aim of adding magnetite was, on one hand, to obtain an intermediate fO_2 via magnetite dissolution in the silicate melts, and on the other hand, to saturate the silicate melts with magnetite. The aim of adding anhydrite was to impose a high fO_2. However, neither magnetite nor anhydrite was found after the experiments because of complete dissolution of magnetite and/or anhydrite in the silicate melts (see below). Furthermore, to reduce the loss of Cu from Cu-Ni-bearing sulfides into the Au capsule walls, a small piece of $Au_{95}Cu_{05}$ alloy was placed at the bottom of each Au capsule of all six experiments. For this set of experiments, the fO_2 was not buffered by any fO_2 buffer, and the run duration ranged from 43 to 46 hours.

The Set-1 to Set-4 experiments were not designed to be fluid-saturated, so the traditional external fO_2 buffers (Chou, 1987), such as used by Jégo and Dasgupta (2014), were not adopted to buffer the experimental fO_2. However, all experiments that were not buffered by any fO_2 buffer were essentially buffered by the combined starting materials and used solid pressure media, although the fO_2 could vary from run to run due to the difference in the starting materials (Prouteau and Scaillet, 2012).

All experiments were conducted in an end-loaded, solid-media piston cylinder apparatus, using 0.5-inch diameter MgO-NaCl assemblies with stepped graphite heaters. All experiments were quenched to below 100 °C within 10-20 s by switching off the electric power to the graphite heaters. The details of the high-pressure equipment and the demonstration of equilibrium partitioning of Au are provided in the Supplementary Materials.

2.3. Analytical methods

Major element compositions of the quenched silicate melts and sulfides (MSS) were measured with a JEOL JXA-8200 electron microprobe, using procedures as described in previous studies (Li and Audétat, 2012, 2013, 2015). The oxidation state of sulfur (S^{6+}/S_{tot}) was determined based on the shift of the SK_α lines with respect to the $BaSO_4$ and ZnS standards (Carroll and Rutherford, 1988), using the same microprobe. Trace element analyses of Au, Cu, Ni, Co, and Ag in the quenched silicate melts and MSS were conducted on an Agilent 7900 Quadrupole ICP-MS coupled to a Photon Machines Analyte HE 193-nm ArF Excimer Laser Ablation system. The detection limit for Au in the quenched silicate melts was ~0.01 ppm. Detailed descriptions of all of the analytical methods are provided in the Supplementary Materials.

3. Results

3.1. Sample petrography

All of the experimental conditions and obtained products are summarized in Table 1. Some representative textures are shown in Fig. 1. A large silicate melt pool was produced in all experiments, and sulfides are present in all experiments where sulfides were added as a starting material. The produced silicate melts and sulfides are the analytical targets of this study. In the Set-1 experiments, the samples contain ~20 to 40% crystals of clinopyroxene ± amphibole ± garnet, and the volume of crystals increases with increasing pressure. In the Set-2 experiments, only a few crystals of clinopyroxene and garnet are present in the hydrous runs at pressures of 2-3 GPa. Graphite is present in all experiments where graphite powder was added as a starting material, and anhydrite is present in all experiments where anhydrite was added, except for run Sulf-3, in which anhydrite was completely dissolved in the silicate melts. In the Set-3 experiments, no silicate crystals were found, and the silicate melts coexist with sulfide ± anhydrite or anhydrite alone. In the Set-4 experiments, only a few crystals of amphibole and/or clinopyroxene are embedded in the silicate melts, but crystals of magnetite and anhydrite were not found because of their complete dissolution in the silicate melts.

In all of the experiments, sulfides are present as Cu-Ni-bearing pyrrhotite (monosulfide solid solution=MSS) or FeS-pyrrhotite crystals (both referred to as MSS hereafter) and were quenched to a homogeneous solid, as indicated by their optical appearance and chemical homogeneity (Fig. 1; Table S3).

3.2. Major element compositions of the silicate melts

Major element contents of all of the quenched silicate melts are listed in Table S2. The produced silicate melts are andesitic to rhyolitic, with NBO/T (=2TotalO/T-4; T=Si+Ti+Al+Cr+P) ranging from 0.012 to 0.441. For the Set-1 and Set-2 experiments, the silicate melt composition deviates from the starting andesite or dacite by showing, in general, lower FeO and MgO contents, which result from partial crystallization. In the Set-3 experiments, the silicate melts that are saturated with MSS are now FeO-rich compared to the starting rhyolitic silicate. The silicate melts that are saturated with both sulfide and anhydrite are a few wt.% higher in FeO than the silicate melts that are saturated with only sulfide but were synthesized under the same *P-T* conditions. The FeO-enrichment in the silicate melts should be caused by oxidation of sulfides during the run. In the Set-4 experiments, the silicate melts of runs C-9a, C-9b, C-10a, and C-10b differ from their starting dacitic and rhyolitic compositions and are now andesitic to dacitic due to magnetite dissolution; while the silicate melts of runs C-10a, C-10b, C-13a, and C-13b became CaO-rich due to anhydrite dissolution. In

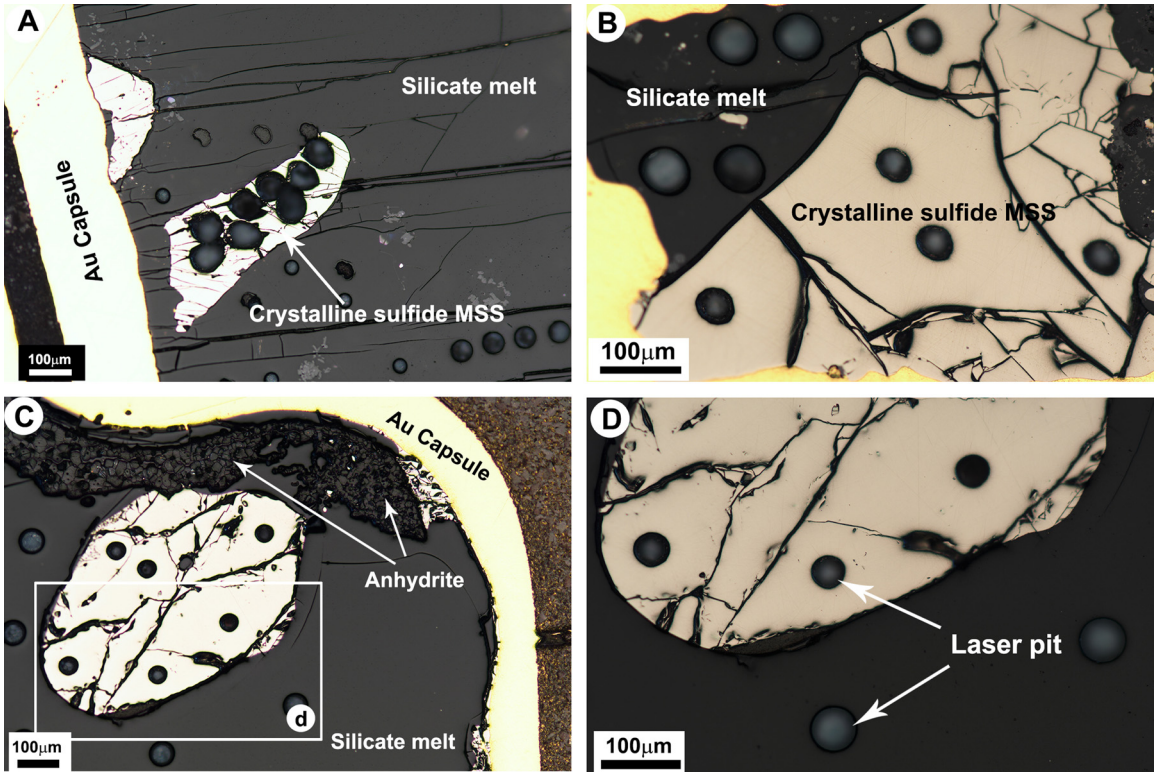

Fig. 1. Reflected-light photomicrographs of typical run products in gold capsules. (A) Run Sulf-4 (1040 °C, 2 GPa, dacitic melt), which shows the coexistence of silicate melt, crystalline sulfide (MSS), and very small silicate crystals. (B) Run Da-3A (1040 °C, 0.5 GPa, dacitic melt), which shows MSS coexisting with silicate melt. (C) Run Rh-1b (1040 °C, 0.5 GPa, rhyolitic melt), which shows the coexistence of silicate melt, crystalline sulfide (MSS), and anhydrite. (D) Close-up view of the crystalline sulfide shown in (C). Note that the crystalline sulfide MSS was quenched into homogeneous solid with a very smooth surface.

addition, the Na_2O content in the silicate melts of the Set-4 experiments is significantly higher than the Na_2O content in the starting silicates. The reason for this is not clear, but the contamination by NaCl-bearing pressure media appears to be impossible because the sample capsules were surrounded by MgO sleeve and spacer. Based on the differences in the EPMA totals to 100 wt.%, the water content in the silicate melts of all present experiments is ~0-12 wt.%, which is generally consistent with the proportion of water added in the starting materials. The water content in the silicate melts of the experiments that simulated slab melting at 1-3 GPa is ~7-12 wt.%.

3.3. Sulfur speciation in the silicate melts and estimation of sample fO_2

The sulfur content in the silicate melts at only sulfide-saturation (SCSS), sulfide-anhydrite-saturation (SCSAS), and only anhydrite-saturation (SCAS) is 40-3000 ppm, 280-5500 ppm, and 50-1030 ppm, respectively (Figs. S2-4). The S^{6+}/S_{tot} in the silicate melts ranges from 0 to 0.96 (Table 1). The S^{6+}/S_{tot} in the only sulfide-saturated silicate melts ranges from 0 to 0.68; whereas in the sulfide-anhydrite-saturated silicate melts it ranges from 0.61 to 0.96. For a given sulfide ± anhydrite and silicate melt system, the measured sulfur content in the silicate melts, in general, increases with increasing S^{6+}/S_{tot} (Fig. S2A), except for the Set-4 experiments. In the Set-4 experiments, the sulfur content in the silicate melts is positively correlated with the Na_2O content (Fig. S2B), which is consistent with the strongly positive effect of Na_2O on SCSS (D'Souza and Canil, 2018).

The fO_2 of most of our experiments was not buffered by any fO_2 buffer. However, the relationship between fO_2 and S^{6+}/S_{tot} in the quenched silicate melts provides an approach to estimate the fO_2 prevailing in our experiments. Several studies have calibrated S^{6+}/S_{tot} in the quenched silicate melts as a function of fO_2 varying from FMQ-2 to FMQ+6 (Carroll and Rutherford, 1988; Jugo et al., 2005; Wallace and Carmichael, 1994) (see (Wilke et al., 2011) for a review), and these calibrations have been used to estimate the fO_2 of natural samples of different compositions by determining S^{6+}/S_{tot} in the sample glasses (Metrich and Clocchiatti, 1996; Rowe et al., 2007; Rowe et al., 2009). In this study, we used a model from Jugo et al. (2005), which was calibrated on a large number of natural and synthetic samples of basaltic to dacitic compositions:

$$S^{6+}/S_{tot} = 1/(1 + 10^{A-B\Delta FMQ}) \quad (3)$$

in which A equals 1.22, B equals 0.95, and ΔFMQ is fO_2 relative to the FMQ buffer. The calculated fO_2 values for our unbuffered experiments that are only sulfide-saturated are between FMQ+0.6 and FMQ+1.6 (Table 1). For the dacitic and rhyolitic experiments that are saturated with both anhydrite and sulfide (Set-2 experiments), the calculated fO_2 values are between FMQ+1.5 and FMQ+2.7 (Table 1).

Several only sulfide-saturated experiments contain graphite (Table 1), and the maximum fO_2 of these experiments corresponds to the C-CO_2 buffer (~FMQ-1.7) (Hirschmann et al., 2008). Therefore, the fO_2 in our only sulfide-saturated experiments is between FMQ-1.7 and FMQ+1.6; while in the experiments that are saturated with both sulfide and anhydrite or anhydrite alone, the fO_2 is between FMQ+1.5 and FMQ+2.7. These fO_2 values are consistent with previous fO_2 values determined for the stabilization of sulfide and/or anhydrite in the andesitic-to-rhyolitic melts (see Parat et al., 2011 for a review). For example, Chang and Audétat (2018) show that their estimated fO_2 values for the andesitic melts that are saturated with both sulfide and anhydrite are between FMQ+2 and FMQ+2.6, which are well consistent with the fO_2 values (FMQ+1.8 to FMQ+2.7) estimated here for our sulfide-anhydrite-saturated dacitic melts. A further evaluation on the va-

lidity of using S^{6+}/S_{tot} in the silicate melts to estimate sample fO_2 is provided in the Supplementary Materials.

In addition, we compared our measured SCSS and SCSAS values with the predicted SCSS values using a comprehensive parameterization of Smythe et al. (2017) (Fig. S3). Fig. S3 shows that our measured SCSS and SCSAS values are generally higher than the predicted SCSS values, which demonstrates that the fO_2 of most of our unbuffered, only sulfide-saturated experiments is in the fO_2 range required for the sulfide-sulfate transition in the silicate melts (see Supplementary Materials). Overall, the present experimental redox conditions well cover those conditions that are relevant for subduction-related magmatism (Frost and McCammon, 2008) and those at which the sulfide-sulfate transition occurs in the silicate melts (Jugo et al., 2005; Jugo et al., 2010).

3.4. Major element compositions of MSS and estimation of sample fS_2

The major element contents of MSS are listed in Table S3. The S and Fe contents in MSS of all sets of experiments range from 36.68 to 39.94 wt.% and from 51.22 to 61.88 wt.%, respectively. The O content in MSS ranges from below 0.2 to 0.7 wt.%, with one sample MSS containing 1.87 wt.% O. The Ni content in the Ni-Cu-bearing MSS ranges from 2.62 to 6.86 wt.%, with most values at ~5 wt.%. The Cu content in the Ni-Cu-bearing MSS ranges from 0.13 to 1.96 wt.%. Compared to the ~2 wt.% Cu in the starting sulfides, significant Cu was thus lost from the Cu-Ni-bearing MSS to the Au capsule walls, except for a few experiments in which a piece of $Au_{95}Cu_{05}$ alloy was added (Table S3). The Cu and Ni contents in FeS-pyrrhotite are low, which are 70-1430 ppm and 17-340 ppm, respectively.

Sample sulfur fugacity $\log fS_2$ was calculated based on the major element compositions of MSS, using an experimental calibration (Toulmin and Barton, 1964):

$$N_{FeS} = FeS/(FeS + S_2) \quad (4)$$

$$\log fS_2 = (70.0 - 85.83N_{FeS}) \times (1000/T - 1) + 39.30\sqrt{(1 - 0.9981N_{FeS})} - 11.91 \quad (5)$$

in which N_{FeS} is the mole fraction of FeS in the FeS-S_2 system, and T is the temperature in K. For all $\log fS_2$ calculations, the measured oxygen in MSS was assumed to be present in the form of FeO, and N_{FeS} was replaced by $N_{FeS+NiS+Cu_2S}$ for the Ni-Cu-bearing MSS (Mengason et al., 2010). The calculated $\log fS_2$ for all of the samples ranges from −2.17 to 2.08 (Table 1). Sample $\log fS_2$ was also calculated using a calibration in which the pressure effect was considered (Froese and Gunter, 1976), but we chose to use the $\log fS_2$ values calculated using the calibration of Toulmin and Barton (1964) (see Supplementary Materials).

3.5. Au solubility in the silicate melts

The solubility of Au in the silicate melts (C_{Au}^{SM}) varies by more than three orders of magnitude, from 0.012 to 55.3 ppm. Although a considerable fraction of sulfur in the only sulfide-saturated silicate melts is present as S^{6+}, as measured by the SK_α method of electron microprobe, C_{Au}^{SM} shows a strong correlation with SCSS (Fig. 2A). However, in the experiments that are sulfide-anhydrite-saturated or only anhydrite-saturated, C_{Au}^{SM} remains nearly constant as the variation of SCSAS or SCAS (Fig. 2A), indicating a negligible role for S^{6+} in enhancing Au dissolution in the silicate melts. Fig. 2B further illustrates that for all of the only sulfide-saturated experiments, $\log(C_{Au}^{SM}$, μmol) is strongly correlated with log(SCSS, μmol), although the sample fO_2 varies from ~FMQ-1.7 to FMQ+1.6 in this study and from ~FMQ-0.5 to FMQ+2

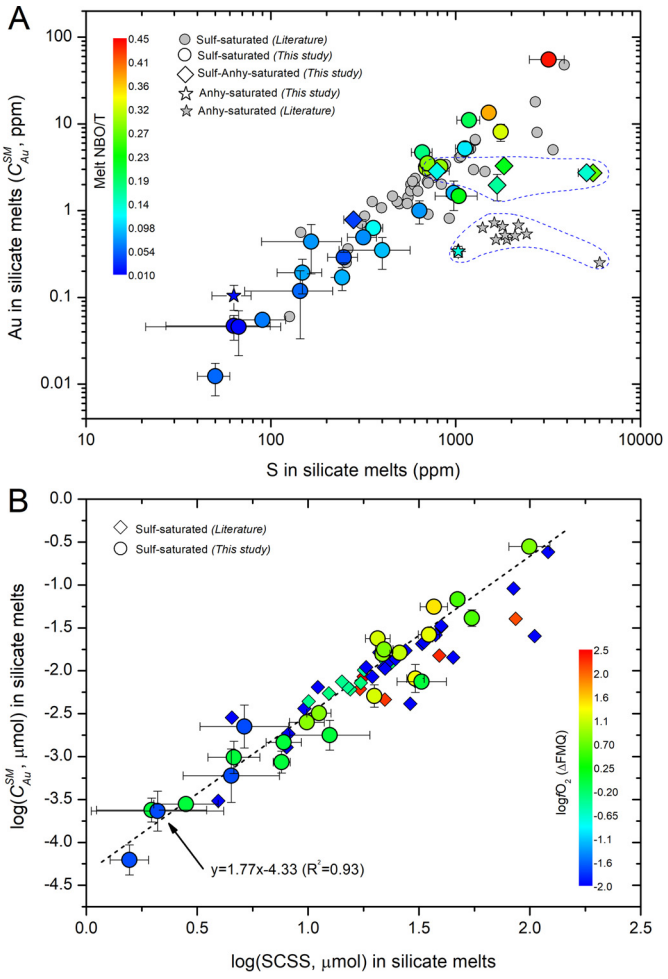

Fig. 2. The solubility of Au in silicate melts (C_{Au}^{SM}) as a function of the melt sulfur content. (A) C_{Au}^{SM} and the melt sulfur content (SCSS) are strongly correlated in the only sulfide-saturated experiments; whereas in the sulfide-anhydrite-saturated or only anhydrite-saturated silicate melts, C_{Au}^{SM} does not vary with the melt sulfur content (SCSAS or SCAS), indicating that S^{6+} does not enhance Au dissolution in the silicate melts. (B) In the only sulfide-saturated experiments, $\log(C_{Au}^{SM}$, μmol) is a strong linear function of log(SCSS, μmol), although the sample fO_2 varies from ~FMQ-1.7 to FMQ+2, which indicates the enhancement of Au dissolution in the silicate melts by the formation of Au-sulfur species at reduced to moderately oxidized conditions. Note that C_{Au}^{SM} and the melt sulfur content are generally higher in the silicate melts with higher NBO/T. The literature data were taken from Zajacz et al. (2013), Botcharnikov et al. (2011), Jégo and Pichavant (2012), and Jégo et al. (2010, 2016).

in previous studies. The correlation between $\log(C_{Au}^{SM}$, μmol) and log(SCSS, μmol) can be described as:

$$\log(C_{Au}^{SM}, \mu mol) = 1.77 \log(SCSS, \mu mol) - 4.33 \ (R^2 = 0.93) \quad (6)$$

These observations are consistent with previous studies (Jégo and Pichavant, 2012; Jégo et al., 2010; Zajacz et al., 2013; Zajacz et al., 2012) that imply the enhancement of C_{Au}^{SM} in S^{2-}-bearing silicate melts. These observations are also consistent with studies of Botcharnikov et al. (2011) and Jégo et al. (2016) that show an increase of C_{Au}^{SM} in the only sulfide-saturated silicate melts with increasing fO_2 over the range of ~FMQ-1.2 to FMQ+2, but the present study more precisely defined the correlation between C_{Au}^{SM} and SCSS due to the largely extended experimental conditions. Jugo et al. (2010) show that over the fO_2 range of sulfide-sulfate transition, the abundance of S^{2-} in the sulfide-saturated silicate melts remains constant, and the increase of SCSS with increasing fO_2 is due to the increased S^{6+} content, which, however, does not complex with Au or enhance Au dissolution (Fig. 2A). Therefore, if the

study of Jugo et al. (2010) is right and if S^{2-} is the only sulfur species that complexes with Au, C_{Au}^{SM} for a given sulfide-saturated silicate melt system should remain constant, regardless of the fO_2 and melt sulfur content. In this context, Fig. 2B implies that in addition to S^{2-}, another sulfur species, which have an intermediate oxidation state and can enhance Au dissolution, may also exist in the only sulfide-saturated silicate melts.

In contrast to Jugo et al. (2010), Botcharnikov et al. (2011) found that the S^{2-} content in the only sulfide-saturated silicate melts increases with increasing fO_2 over the range of FMQ-0.5 to FMQ+1.5. If this finding is correct, then the observation that C_{Au}^{SM} is positively correlated with SCSS over the fO_2 range of ~FMQ-1.7 to FMQ+2 (Fig. 2B) could be explained by the formation of only Au-sulfide species in the silicate melts (Jégo et al., 2016). Species such as Au-Na/H-S (Zajacz et al., 2013) and Au_2-Fe-S_2 (Jégo and Pichavant, 2012) have been proposed to be the main Au-sulfide species in the silicate melts. However, the slope of 1.77 of Eq. (3), derived from experiments performed under different conditions of P-T-fO_2-melt composition, indicates that the Au-S species dissolved in the silicate melts may be more complicated than these. The actual sulfur and Au-S species dissolved in the sulfide-saturated silicate melts at different fO_2s await future in-situ spectroscopic measurements; however, more importantly, C_{Au}^{SM} is strongly correlated with SCSS in the only sulfide-saturated silicate melts over an fO_2 range of ~FMQ-1.7 to FMQ+2 (Fig. 2B).

3.6. Au solubility in MSS

The solubility of Au in MSS (C_{Au}^{MSS}) varies from 130 to 2800 ppm and is positively correlated with the sample $\log fS_2$ (Fig. 3). The presence or absence of several wt.% of Ni and Cu in MSS appears not to affect C_{Au}^{MSS} (Fig. 3A).

The dissolution of Au in MSS can be described by a reaction of

$$\text{Au (metal)} + \frac{1}{4}S_2 = \text{AuS}_{1/2}\ \text{(MSS)} \quad (7)$$

Since the activity of Au in pure Au-metal is one, the equilibrium constant (K) of Eq. (7) can be written as:

$$K = \frac{\alpha AuS_{1/2}}{f^{1/4}S_2} \quad (8)$$

which can be further arranged as:

$$\log K = \log \alpha \text{AuS}_{1/2} - 1/4 \log fS_2 \quad (9)$$

$$\log \gamma \text{AuS}_{1/2} X\text{AuS}_{1/2} = 1/4 \log fS_2 + \log K \quad (10)$$

In Eqs. (8)–(10), α, γ, and X refer to the activity, activity coefficient, and mole fraction of Au in MSS. Assuming that $\gamma \text{AuS}_{1/2}$ does not change greatly with the temperature and small variation of MSS composition, Eq. (10) can be further written as:

$$\log(C_{Au}^{MSS}, ppm) = 1/4 \log fS_2 + C \quad (11)$$

in which C is a constant. Eq. (11) would imply that $\log(C_{Au}^{MSS}, ppm)$ increases with increasing $1/4 \log fS_2$, which is in a good agreement with the trend shown in Fig. 3B.

3.7. MSS-silicate melt partitioning of Au

The Nernst partition coefficient $D_{Au}^{MSS/SM}$, calculated from Au weight proportions in MSS and silicate melt, varies by more than three orders of magnitude, from 10 to 14000 (Fig. 4). Negative correlations exist between $D_{Au}^{MSS/SM}$ and the melt sulfur or Au content for all of the only sulfide-saturated experiments over the fO_2 range of ~FMQ-1.7 to FMQ+1.6 (Fig. 4). However, for the sulfide-anhydrite-saturated experiments, $D_{Au}^{MSS/SM}$ does not show any dependence on the melt sulfur content, which again indicates that the dissolved S^{6+} does not enhance Au dissolution in the silicate melts. These experimental results thus reveal that the MSS-silicate melt partitioning of Au under reduced to moderately oxidized conditions ($fO_2 \leqslant$FMQ+1.6) depends significantly on SCSS. According to Fig. 4A, $D_{Au}^{MSS/SM}$ can be directly linked to SCSS in a quantitative way, as follows:

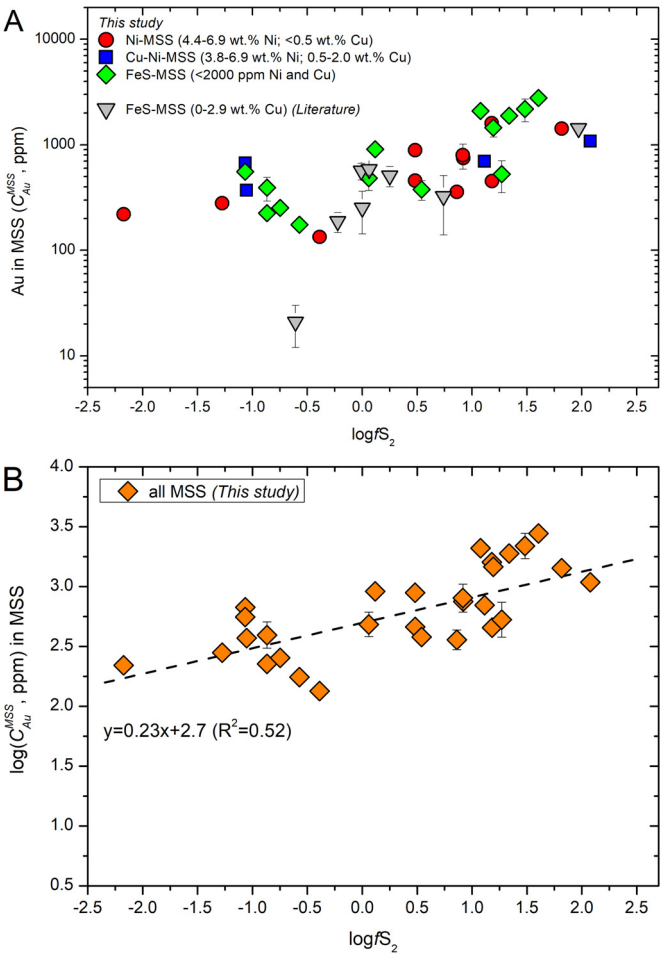

Fig. 3. The solubility of Au in monosulfide-solid-solution (C_{Au}^{MSS}) as a function of sulfur fugacity $\log fS_2$. Note that C_{Au}^{MSS}, in general, increases with increasing $\log fS_2$, and C_{Au}^{MSS} is not considerably affected by the presence of different amounts of Ni and Cu in MSS. The literature data were taken from Botcharnikov et al. (2011) and Zajacz et al. (2013).

$$\log D_{Au}^{MSS/SM} = -1.63 \log(\text{SCSS, ppm}) + 7.03\ (R^2 = 0.86) \quad (12)$$

In addition, the combination of Eq. (6) and Eq. (11) by converting μmol into ppm in Eq. (6) would yield:

$$\log(C_{Au}^{MSS}, \text{ ppm}) - \log(C_{Au}^{SM}, \text{ ppm}) = 0.25 \log fS_2 - 1.77 \log(\text{SCSS, ppm}) + C \quad (13)$$

In Eq. (13), $\log(C_{Au}^{MSS}, \text{ ppm}) - \log(C_{Au}^{SM}, \text{ ppm})$ equals $\log D_{Au}^{MSS/SM}$, so Eq. (13) can be further written as:

$$\log D_{Au}^{MSS/SM} = 0.25 \log fS_2 - 1.77 \log(\text{SCSS, ppm}) + C \quad (14)$$

Eq. (14) implies that $D_{Au}^{MSS/SM}$ should be a function of fS_2 and SCSS. Regression of our $\log D_{Au}^{MSS/SM}$ data as a multiple linear function of $\log fS_2$ and log(SCSS, ppm) yielded:

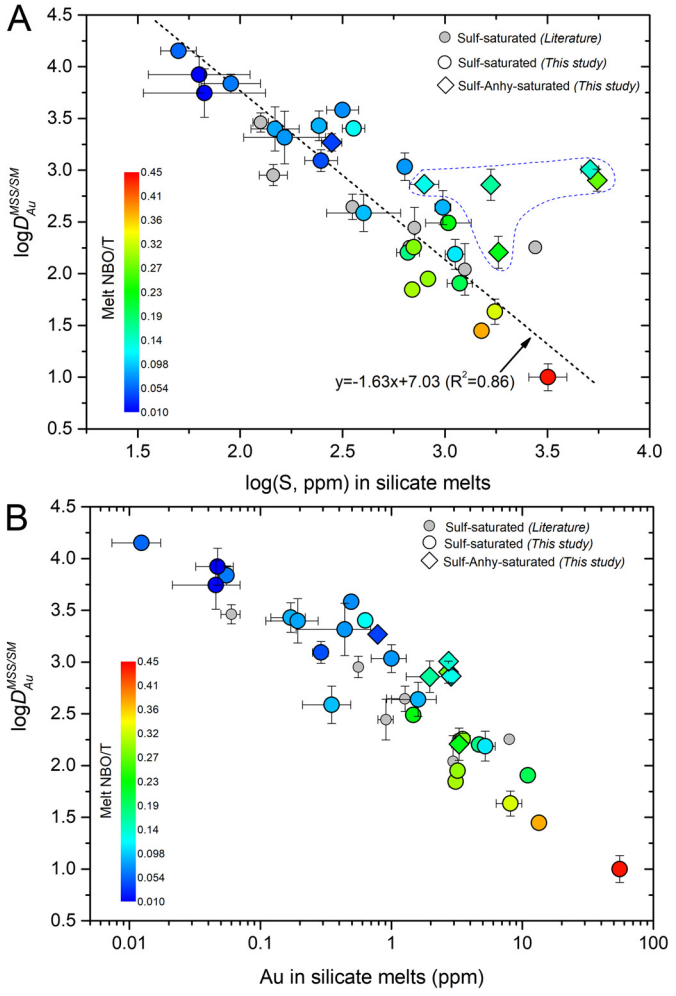

Fig. 4. MSS-silicate melt partition coefficient of Au ($D_{Au}^{MSS/SM}$) as a function of the melt sulfur/Au content for the only sulfide-saturated and sulfide-anhydrite-saturated experiments. (A) For the only sulfide-saturated experiments under reduced to moderately oxidized conditions (FMQ-1.7 < fO_2 < FMQ+1.6), the correlation between $D_{Au}^{MSS/SM}$ and the melt sulfur content (SCSS) can be described as $\log D_{Au}^{MSS/SM} = -1.63\log(\text{SCSS, ppm}) + 7.03$ ($R^2 = 0.86$). The independence of $D_{Au}^{MSS/SM}$ on the melt sulfur content (SCSAS) in the sulfide-anhydrite-saturated experiments indicates that S^{6+} does not enhance Au dissolution in the silicate melts, as explained in Fig. 2A. (**B**) $\log D_{Au}^{MSS/SM}$ is strongly negatively correlated with the melt Au content for all sulfide-saturated and sulfide-anhydrite-saturated experiments. Note that $D_{Au}^{MSS/SM}$ varies by more than three orders of magnitude, and $D_{Au}^{MSS/SM}$ is generally lower for the experiments with higher NBO/T. The literature data were taken from Botcharnikov et al. (2011) and Zajacz et al. (2013).

$$\log D_{Au}^{MSS/SM} = 0.27\log fS_2 - 1.64\log(\text{SCSS, ppm}) + 7.03\ (R^2 = 0.94) \quad (15)$$

The coefficients for $\log fS_2$ and log(SCSS, ppm) in Eqs. (14) and (15) are nearly identical. Accordingly, the large variation of $D_{Au}^{MSS/SM}$ observed in this study appears to be fully explained by the combined fS_2 and SCSS, but $D_{Au}^{MSS/SM}$ depends more heavily on SCSS. To further test the model of Eq. (15), all present and literature $D_{Au}^{MSS/SM}$ data (total data points $n = 49$ as compiled in Fig. S1) were fitted as a multiple linear function of fS_2 and SCSS, which yielded:

$$\log D_{Au}^{MSS/SM} = 0.28\log fS_2 - 1.23\log(\text{SCSS, ppm}) + 5.89\ (R^2 = 0.74) \quad (16)$$

A comparison between the experimentally measured $\log D_{Au}^{MSS/SM}$ and the predicted $\log D_{Au}^{MSS/SM}$ using Eq. (16) is provided in Fig. S5, which illustrates that more than 90% of the $\log D_{Au}^{MSS/SM}$ data can be predicted within 0.5 log units.

4. Discussion

4.1. Factors that affect the MSS-silicate melt partitioning of Au

The above results, as summarized in Fig. 4A and Eqs. (12) and (15), demonstrate that the melt sulfur content (SCSS) and fS_2 strongly control the MSS-silicate melt partitioning of Au under reduced to moderately oxidized conditions. However, SCSS is a multiple function of the temperature, pressure, fO_2, melt composition, and melt water content (Jugo et al., 2010; Smythe et al., 2017), and fS_2 is positively correlated with fO_2 in fS_2-unbuffered, sulfide-saturated experiments (Botcharnikov et al., 2011; Li and Audétat, 2012). The SCSS at fO_2 of the sulfide-sulfate transition is up to one order of magnitude higher than the SCSS at fO_2 below FMQ (Jugo et al., 2010). Mafic-to-intermediate melts, in general, have higher SCSS than the felsic melts (Clemente et al., 2004), and alkaline melts have particularly high SCSS as shown in Fig. S2 and by D'Souza and Canil (2018). For a hydrous melt of basaltic andesite at 1250 °C and 1 GPa, increasing per wt.% of Na_2O would increase the SCSS by ~560 ppm (D'Souza and Canil, 2018); increasing the per wt.% of H_2O would increase the SCSS by ~100 ppm in the basaltic to rhyolitic melts (Fortin et al., 2015). Therefore, the sulfide-silicate melt partitioning of Au is indirectly controlled by all of the factors that control the SCSS and fS_2. The large variation of $D_{Au}^{MSS/SM}$ from 10 to 14000, as compiled in Fig. S1, can be indirectly ascribed to the variation of physical and chemical parameters such as the experimental temperature, pressure, fO_2, silicate melt composition, and melt water content, because a variation of any of these parameters can cause a variation in SCSS and, consequently, a variation in $D_{Au}^{MSS/SM}$. For example, the $D_{Au}^{MSS/SM}$ values obtained from the sulfide-andesitic melt system are lower than those obtained from the sulfide-rhyolitic melt system because of the higher SCSS in andesitic melts (Fig. 4A). For a given sulfide-silicate melt system, the $D_{Au}^{MSS/SM}$ values obtained under moderately oxidized conditions are lower than those obtained under reduced conditions because of the enhanced SCSS under moderately oxidized conditions (Table 1). Apparently, the $D_{Au}^{MSS/SM}$ for hydrous and moderately oxidized mafic to intermediate melts could be sufficiently low owing to the large SCSS, in such a way that fractionation of MSS may sequester very limited amounts of Au. Whereas, fractionation of a small amount of MSS could potentially sequester most of the Au for a rhyolitic system owing to the small SCSS (see below).

The sulfide-silicate melt partitioning of many chalcophile elements, such as Ni, Re, Mo, and Pb, is a strong function of the melt FeO content or both the melt FeO content and fO_2, as summarized by Eqs. (1) and (2) and discussed previously, because these metals dissolve as different metal oxide species in the silicate melts (Feng and Li, 2019; Kiseeva and Wood, 2013, 2015; Li, 2014; Li and Audétat, 2012, 2015). Eqs. (6), (12), and (15), and Figs. 2 and 4 as well, demonstrate that, compared to many other chalcophile elements, Au has a remarkably distinct dissolution mechanism in the sulfide-saturated silicate melts (mainly as Au-S species) and, consequently, a distinct partitioning behavior in the sulfide-silicate melt systems. Eqs. (12) and (15) also explain the observed lack of correlation between $D_{Au}^{MSS/SM}$ and the melt FeO content or fO_2 (Fig. S1), because neither the melt FeO content nor fO_2 is the only factor that determines SCSS and/or fS_2 (Jugo et al., 2010; Smythe et al., 2017).

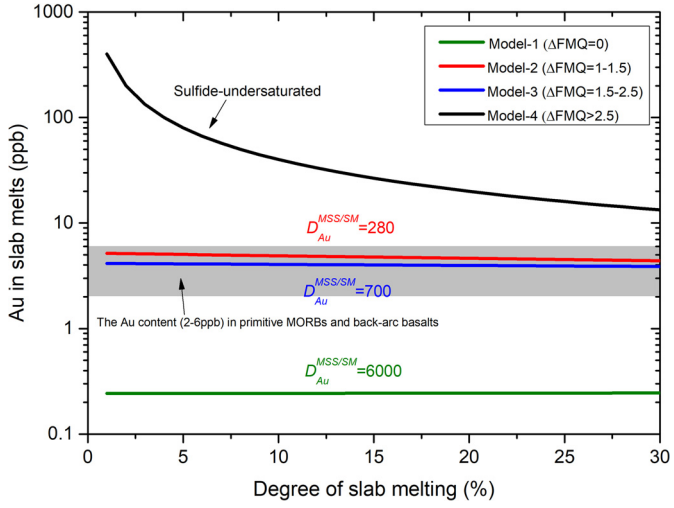

Fig. 5. Modeled Au content in the slab melts as a function of the degree of slab melting at various redox states using a batch melting model. The Au content in primitive MORBs and back-arc basalts (Jenner et al., 2010) was taken for comparison with the modeled Au content in the slab melts. The fO_2 during slab melting increases from Model-1 to Model-4. The slab melting temperature is assumed to be 1000 °C, under which condition most of the experiments were performed to determine the SCSS in the slab melts (Fig. S4). See text for a detailed description of each model calculation.

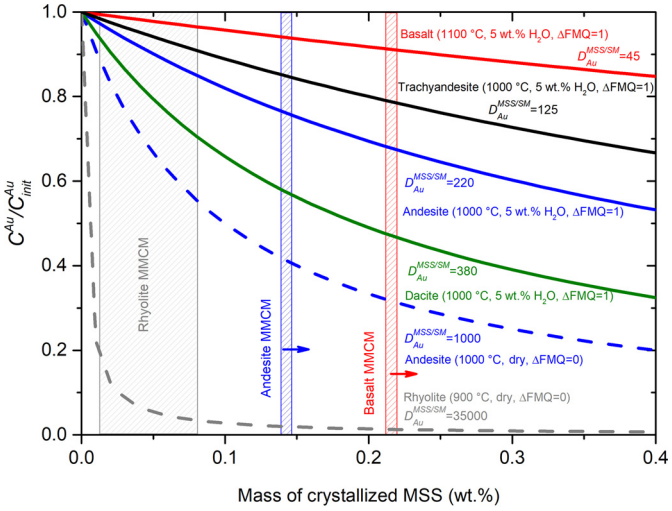

Fig. 6. Variation of the Au content in arc magmas induced by MSS crystallization. Equilibrium crystallization of MSS is used for all of the calculations. The model of D'Souza and Canil (2018) was used for calculating the SCSS in trachyandesite at 0.2 GPa, and the SCSS for other types of arc magmas is calculated at 0.2 GPa using the model of Smythe et al. (2017). For magmas at fO_2 of FMQ+1, the melt sulfur content equals twice the calculated SCSS owing to the positive effect of fO_2 on SCSS (Botcharnikov et al., 2011; Jugo et al., 2010); otherwise it equals the calculated SCSS. $D_{Au}^{MSS/SM}$ is calculated for each type of arc magma using the melt sulfur content and Eq. (12) by assuming $\log fS_2 = 0$. The maximum mass of crystallized MSS (MMCM) for each type of magma is defined based on the observed range of sulfur contents in the corresponding arc magma (50-300 ppm for rhyolite, 500-2000 ppm for andesite, and 800-3000 ppm for basalt) (Wallace and Edmonds, 2011), by assuming that all sulfur in the magma crystallized as FeS-sulfide. The arrows mean that the MMCM for andesite and basalt is larger than the dashed area due to the large range of sulfur contents in arc andesite and basalt. C^{Au}/C_{init}^{Au} denotes ratio of the Au content in the magma after and before MSS crystallization. Note that the small effect of MSS crystallization on the Au content in moderately oxidized mafic to intermediate magmas with a high-water content is due to the high sulfur content in the silicate melt.

4.2. Fate of Au during slab melting and deep Au cycle

The above results can be used to constrain the fate of Au during slab melting and the deep Au cycle in subduction zones via modelling the efficiency of Au extraction by slab melts. The redox state of the altered oceanic crust plus sediments could have plausibly varied from being reduced to oxidized through geological time (Evans and Tomkins, 2011), so we considered four different slab melting models to calculate the Au content in the slab melts (Fig. 5). In each model, concentrations of 1000 ppm sulfur and 4 ppb Au were assumed in the slab as in the primitive MORBs (Jenner et al., 2010). In Model-1, the slab fO_2 is ~FMQ, and SCSS in the slab melts is ~100 ppm, as determined at 850-1050 °C and 2-3 GPa (Jégo and Dasgupta, 2013, 2014), which correspond to a $D_{Au}^{MSS/SM}$ value of ~6000 (Fig. 4A; Eq. (12)), while sulfur is present as pyrrhotite in the slab (Jégo and Dasgupta, 2013). In Model-2, the slab is moderately oxidized, with fO_2 between FMQ+1 and FMQ+1.5, and SCSS in the slab melts is ~700 ppm, as determined in this study and Jégo and Dasgupta (2014) (Fig. S4), which correspond to a $D_{Au}^{MSS/SM}$ value of ~280, while the sulfur is still present as pyrrhotite. We also considered one highly oxidized model (Model-3; FMQ+1.5< fO_2 <FMQ+2.5). In Model-3, we assumed that half of the slab sulfur is sulfide and the other half is sulfate during slab melting, despite the fact that the coexistence of sulfide and sulfate minerals in modern altered oceanic crust (Alt and Shanks, 2011; Evans, 2012) does not necessarily mean the presence of this much sulfate during slab melting. In this model, the minimum $D_{Au}^{MSS/SM}$ value (700) of those obtained from the sulfide-anhydrite-saturated experiments at 2 GPa is used (Table 1). In Model-4, the slab fO_2 is assumed to be exceedingly high (fO_2 >FMQ+2.5), in such a way that only sulfate is present during slab melting. In this model, Au is thought to be perfectly incompatible during slab melting due to the absence of sulfides. Fig. 5 shows that the calculated Au content in the slab melts from Model-1 to Model-3 is below 5 ppb, and efficient Au extraction by slab melts occurs only when all of the sulfur is present as sulfate during slab melting (Model-4).

Fig. 5 illustrates that slab melts of both ancient (>2.5 Ga) and modern subduction zones can transport less than 25% of slab Au to the subarc mantle, if the degree of slab melting is not higher than 20%. Before the rise of oxygen in Earth's atmosphere at ~2.2-2.5 Ga (Lyons et al., 2014), sulfur occurs mainly as sulfide in the altered oceanic crust and the fO_2 during slab melting is not higher than FMQ (Evans and Tomkins, 2011; Prouteau and Scaillet, 2012). Therefore, partial melting of the ancient slab must lead to a negligible transfer of slab Au and sulfur to the subarc mantle due to the very small SCSS in the slab melts (Model-1 of Fig. 5). The redox state of the modern subducting slab remains debated. The oxidized nature of arc magmas could be inherited from oxidized materials of the subducting slab (Kelley and Cottrell, 2009; Mungall, 2002); however, similar V/Sc and Fe/Zn systematics in primitive MORBs and arc basalts suggest that the subducting slab may not be more oxidized than the oceanic mantle ($fO_2 \leqslant$FMQ) (Lee et al., 2005; Lee et al., 2010). Anhydrite together with pyrite was found in fluid inclusions of eclogitic vein assemblages (Zhang et al., 2008); whereas there are lines of evidence for the ubiquitous presence of sulfides in subduction-related eclogites (Aulbach et al., 2012; Evans et al., 2014). The sulfide abundance is much greater than the sulfate abundance in modern altered oceanic crust (Alt and Shanks, 2011; Evans, 2012), which is suggestive of more sulfur in the reduced species that enter the subduction zones. Because pressure causes the reduction of an iso-chemical silicate assemblage (Stagno et al., 2013), most of the sulfur present during slab melting at the subarc depth could be in the form of pyrrhotite and subducted efficiently into the deep mantle (Jégo and Dasgupta, 2013), which well explains the imbalance between the sulfur input and output in modern subduction zones - more than two thirds of the sulfur in modern subduction zones entering the deep mantle but not sourced by arc volcanism (Evans, 2012; Jégo and Dasgupta, 2013).

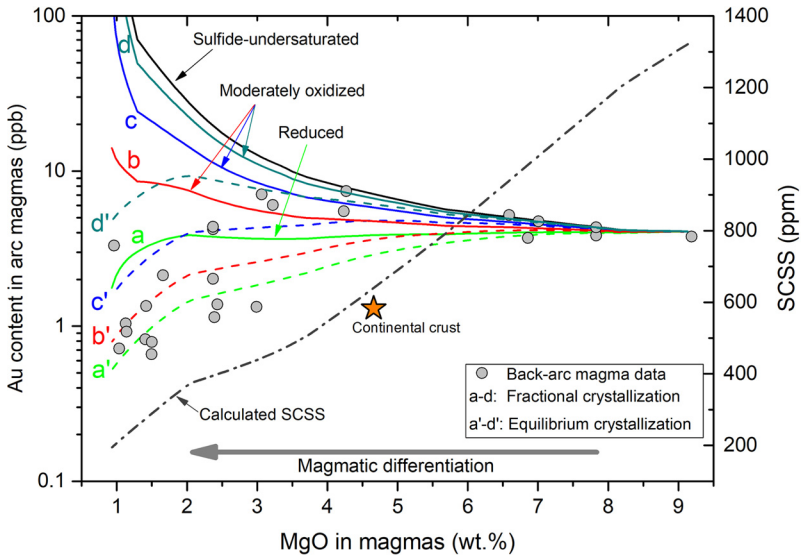

Fig. 7. Modeled Au content in MSS-saturated arc magmas differentiating from a MORB-like basalt with 2 wt.% water to a felsic residual magma. The magmatic differentiation trend was modeled from 1200 °C and 0.4 GPa using Rhyolite-MELTS (Gualda et al., 2012), and the modeled major elements were used to calculate the SCSS (dot-and-dash dark curve) in silicate melts of the differentiating arc magmas, using the model of Smythe et al. (2017). For differentiation under reduced conditions (fO_2=FMQ) (a-a' curves), the melt sulfur content equals the calculated SCSS; whereas, for differentiation under moderately oxidized conditions (FMQ<fO_2<FMQ+1.5), it equals two times (b-b' and c-c' curves) and four times (d-d' curves) the calculated SCSS, by assuming 50% and 25% of sulfur present as S^{2-} in the moderately oxidized silicate melts, respectively. The corresponding $D_{Au}^{MSS/SM}$ used for modeling was calculated using the melt sulfur content and Eq. (12). A content of 4 ppb Au was assumed in the initial MORB-like basalt (Jenner et al., 2010). The mass of crystallized MSS for each step of crystallization was determined by variation of the calculated SCSS for a-a', c-c', and d-d' curves and by variation of twice the calculated SCSS for b-b' curves, by assuming that all sulfur is removed as FeS-sulfide. Note that for b-b' curves, all of the sulfur, including S^{2-} and S^{6+}, is removed as FeS-sulfide, which could be caused by magnetite crystallization (Jenner et al., 2010) and/or degassing (Moussallam et al., 2016) for example. The modeled Au content in sulfide-undersaturated differentiating magmas, and the Au content in the continental crust (Rudnick and Gao, 2014) and back-arc magmas of the Eastern Manus basin (Jenner et al., 2010; Sun et al., 2004) were plotted for comparison.

Therefore, the extreme case, Model-4 of Fig. 5, cannot be realistic for any of the subduction zones. In addition, even if the slab is moderately oxidized or highly oxidized, as assumed in Model-2 and Model-3, the calculated Au content in the slab melts is not higher than the Au content in the primitive MORBs and arc basalts (Fig. 5). Accordingly, Fig. 5 implies that, although the capacity of slab melts in transporting Au depends on fO_2, the slab melts of both ancient and modern subduction zones overall have a low capacity in transporting slab Au to the subarc mantle. A low capacity for slab melts in transporting Au would imply that most of the slab Au which is coupled with sulfides is subducted into the deep mantle, and the slab melts contribute insignificant Au to the arc basalts. The observation (Jenner et al., 2010) that subduction-related, back-arc basalts have similar Au contents as MORBs may corroborate these conclusions, although the slab fluids thus far cannot be excluded from being a medium to transfer slab Au to the subarc mantle.

4.3. Au-enrichment and ore potential of MSS-saturated arc magmas

Our partitioning data also provide new constraints on the Au-enrichment and ore potential of the differentiating arc magmas. The depletion of Cu in variously evolved arc magmas and the continental crust indicates the fractionation of MSS during arc magmatic differentiation (Jenner, 2017; Lee et al., 2012; Li, 2014; Li and Audétat, 2013; Wang et al., 2018). To evaluate the effect of the fractionation of MSS on the Au content in the differentiating arc magmas, we have calculated the Au content in silicate melts of various compositions, melt water contents, and oxidation states as a function of the mass of crystallized MSS (Fig. 6). Fig. 6 illustrates that MSS crystallization has a very limited effect on the Au content in moderately oxidized mafic to intermediate magmas with high-water contents, but the effect can be significant for dry and reduced magmas, felsic magmas in particular. In addition, the Au content in the alkaline magmas (trachyandesite) appears to be less affected by MSS crystallization compared to the normal andesite, which can be ascribed to the higher SCSS caused by the higher Na_2O+K_2O content in trachyandesite (D'Souza and Canil, 2018). To further investigate the effect of fractionation of MSS on the Au content in the differentiating hydrous arc magmas under reduced to moderately oxidized conditions, we have also calculated the SCSS and the corresponding $D_{Au}^{MSS/SM}$ for a series of magmas, differentiating from basaltic to granitic compositions at the saturation of MSS; the calculated SCSS and $D_{Au}^{MSS/SM}$ values were then used to calculate the Au content in the differentiating magmas as a function of MgO (Fig. 7). Fig. 7 shows that MSS crystallization would not cause depletion of Au in hydrous mafic-to-intermediate magmas (>3 wt.% MgO) under moderately oxidized conditions, and Au prefers to accumulate in the residual magmas if the magmatic crystallization follows a fractional crystallization model. Though not shown in Fig. 7, the enrichment of Au in the residual arc magmas can be further enhanced if the magmas are rich in alkali metals, because the oxides of alkali metals in magmas can significantly increase SCSS but decrease $D_{Au}^{MSS/SM}$ as discussed above and shown in Fig. S2B. Fig. 7 also illustrates that sulfide-undersaturation would sufficiently cause Au-enrichment in the differentiating arc magmas, but it is not a necessary condition to generate Au-enrichment. Previous studies (Mungall, 2002; Sillitoe, 1997) suggest that exceedingly high fO_2 is required to generate Au-enrichment in magmas via suppressing the saturation of sulfides; however, it should be noted that sulfide-saturation is a globally common phenomenon in arc magmas of mafic-to-felsic compositions (Chiaradia, 2014; Lee et al., 2012).

The above results (Figs. 6 and 7) have important implications for the formation of magmatic-hydrothermal Au deposits. The magmas that are formed under moderately oxidized conditions and that have high contents of sulfur, alkali metal, and water would potentially have a high content of Au. In an aqueous fluid-magma system under moderately oxidized conditions, Au complexed with sulfur partitions strongly into the fluid phase

(Zajacz et al., 2012), particularly when the aqueous fluids are rich in alkali metals and chlorine (Zajacz et al., 2010). Therefore, Au, sulfur, water, chlorine, and alkali metals are indeed interplayed in a moderately oxidized aqueous fluid-magma system. All of the factors that favor the formation of Au-enrichment in the magmas would essentially favor the magma to fluid transfer of Au and consequently, the formation of Au-enrichment in the aqueous fluids. Accordingly, the mafic to intermediate hydrous magmas, alkaline magmas in particular, under moderately oxidized conditions would have a high potential to form magmatic-hydrothermal Au deposits. These findings explain the strong genetic link observed between large to giant Au deposits and alkaline magmas (Müller and Groves, 2016; Sillitoe, 1997; Sillitoe, 2002), which are a type of magmas that are generated by small degrees of partial melting of the metasomatized subarc mantle and show high contents of alkali metals, sulfur, water, chlorine, and Au (D'Souza and Canil, 2018; Li and Audétat, 2013; Müller and Groves, 2016).

It is worthwhile to further point out that, although an exceedingly high fO_2 does render high Au contents in the differentiating magmas via suppressing sulfide-saturation (Fig. 7), it does not favor an efficient magma-to-fluid transfer of Au, which may hinder the formation of magmatic-hydrothermal Au deposits. This is because sulfur occurring as oxidized species (*e.g.*, SO_2) in oxidized fluids does not favor the partitioning of Au into the aqueous fluids (Zajacz et al., 2012; Zajacz et al., 2010). In addition, although Au-enrichment can also occur in moderately oxidized felsic magmas (<1.5 wt.% MgO, >70 wt.% SiO_2; Fig. 7) if the crystallization follows the fractional crystallization model, the low sulfur contents or SCSS of these magmas, as observed in natural felsic arc magmas (Wallace and Edmonds, 2011) and shown in Fig. 7, may limit their potential to form magmatic-hydrothermal Au deposits of large-to-giant sizes.

Acknowledgements

This project was supported by the Strategic Priority Research Program (B) of the Chinese Academy of Sciences (XDB18020301), the Recruitment Program of Global Young Experts (P.R. China) to YL and NERC grant NE/L010828/1 to ESK. Constructive reviews by Zoltan Zajacz, Sébastien Jégo, and an anonymous reviewer helped to improve this paper. The effective handling of this paper by Frederic Moynier is appreciated.

Appendix A. Supplementary material

Supplementary material related to this article can be found online at https://doi.org/10.1016/j.epsl.2019.115850.

References

Alard, O., Lorand, J.P., Reisberg, L., Bodinier, J.L., Dautria, J.M., O'Reilly, S.Y., 2011. Volatile-rich metasomatism in montferrier xenoliths (southern France): implications for the abundances of chalcophile and highly siderophile elements in the subcontinental mantle. J. Petrol. 52, 2009–2045.

Alt, J.C., Shanks, W.C., 2011. Microbial sulfate reduction and the sulfur budget for a complete section of altered oceanic basalts, IODP hole 1256D (eastern Pacific). Earth Planet. Sci. Lett. 310, 73–83.

Aulbach, S., Stachel, T., Seitz, H.-M., Brey, G.P., 2012. Chalcophile and siderophile elements in sulphide inclusions in eclogitic diamonds and metal cycling in a paleoproterozoic subduction zone. Geochim. Cosmochim. Acta 93, 278–299.

Bockrath, C., Ballhaus, C., Holzheid, A., 2004. Fractionation of the platinum-group elements during mantle melting. Science 305, 1951–1953.

Botcharnikov, R.E., Holtz, F., Mungall, J.E., Beermann, O., Linnen, R.L., Garbe-Schonberg, D., 2013. Behavior of gold in a magma at sulfide-sulfate transition: revisited. Am. Mineral. 98, 1459–1464.

Botcharnikov, R.E., Linnen, R.L., Wilke, M., Holtz, F., Jugo, P.J., Berndt, J., 2011. High gold concentrations in sulphide-bearing magma under oxidizing conditions. Nat. Geosci. 4, 112–115.

Canil, D., Fellows, S.A., 2017. Sulphide–sulphate stability and melting in subducted sediment and its role in arc mantle redox and chalcophile cycling in space and time. Earth Planet. Sci. Lett. 470, 73–86.

Carroll, M., Rutherford, M.J., 1988. Sulfur speciation in hydrous experimental glasses of varying oxidation state–results from measured wavelength shifts of sulfur X-rays. Am. Mineral. 73, 845–849.

Chang, J., Audétat, A., 2018. Petrogenesis and metal content of hornblende-rich xenoliths from two laramide-age magma systems in southwestern USA: insights into the metal budget of arc magmas. J. Petrol. 59, 1869–1898.

Chiaradia, M., 2014. Copper enrichment in arc magmas controlled by overriding plate thickness. Nat. Geosci. 7, 43–46.

Chou, I.-M., 1987. Oxygen buffer and hydrogen sensor techniques at elevated pressures and temperatures. Hydrother. Exp. Tech., 61–99.

Clemente, B., Scaillet, B., Pichavant, M., 2004. The solubility of sulphur in hydrous rhyolitic melts. J. Petrol. 45, 2171–2196.

D'Souza, R., Canil, D., 2018. Effect of alkalinity on sulfur concentration at sulfide saturation in hydrous basaltic andesite to shoshonite melt at 1270 °C and 1 GPa. Am. Mineral. 103, 1030–1043.

Evans, K.A., 2012. The redox budget of subduction zones. Earth-Sci. Rev. 113, 11–32.

Evans, K.A., Tomkins, A.G., 2011. The relationship between subduction zone redox budget and arc magma fertility. Earth Planet. Sci. Lett. 308, 401–409.

Evans, K.A., Tomkins, A.G., Cliff, J., Fiorentini, M.L., 2014. Insights into subduction zone sulfur recycling from isotopic analysis of eclogite-hosted sulfides. Chem. Geol. 365, 1–19.

Feng, L., Li, Y., 2019. Comparative partitioning of Re and Mo between sulfide phases and silicate melt and implications for the behavior of Re during magmatic processes. Earth Planet. Sci. Lett. 517, 14–25.

Fortin, M.-A., Riddle, J., Desjardins-Langlais, Y., Baker, D.R., 2015. The effect of water on the sulfur concentration at sulfide saturation (SCSS) in natural melts. Geochim. Cosmochim. Acta 160, 100–116.

Froese, E., Gunter, A.E., 1976. A note on the pyrrhotite-sulfur vapor equilibrium. Econ. Geol. 71, 1589–1594.

Frost, D.J., McCammon, C.A., 2008. The redox state of Earth's mantle. Annu. Rev. Earth Planet. Sci. 36, 389–420.

Gualda, G.A.R., Ghiorso, M.S., Lemons, R.V., Carley, T.L., 2012. Rhyolite-MELTS: a modified calibration of MELTS optimized for silica-rich, fluid-bearing magmatic systems. J. Petrol. 53, 875–890.

Hirschmann, M.M., Ghiorso, M.S., Davis, F.A., Gordon, S.M., Mukherjee, S., Grove, T.L., Krawczynski, M., Medard, E., Till, C.B., 2008. Library of experimental phase relations (LEPR): a database and web portal for experimental magmatic phase equilibria data. Geochem. Geophys. Geosyst. 9.

Jégo, S., Dasgupta, R., 2013. Fluid-present melting of sulfide-bearing ocean-crust: experimental constraints on the transport of sulfur from subducting slab to mantle wedge. Geochim. Cosmochim. Acta 110, 106–134.

Jégo, S., Dasgupta, R., 2014. The fate of sulfur during fluid-present melting of subducting basaltic crust at variable oxygen fugacity. J. Petrol. 55, 1019–1050.

Jégo, S., Nakamura, M., Kimura, J.-I., Iizuka, Y., Chang, Q., Zellmer, G.F., 2016. Is gold solubility subject to pressure variations in ascending arc magmas? Geochim. Cosmochim. Acta 188, 224–243.

Jégo, S., Pichavant, M., 2012. Gold solubility in arc magmas: experimental determination of the effect of sulfur at 1000 °C and 0.4 GPa. Geochim. Cosmochim. Acta 84, 560–592.

Jégo, S., Pichavant, M., Mavrogenes, J.A., 2010. Controls on gold solubility in arc magmas: an experimental study at 1000 °C and 4 kbar. Geochim. Cosmochim. Acta 74, 2165–2189.

Jenner, F.E., 2017. Cumulate causes for the low contents of sulfide-loving elements in the continental crust. Nat. Geosci.

Jenner, F.E., O'Neill, H.S.C., Arculus, R.J., Mavrogenes, J.A., 2010. The magnetite crisis in the evolution of arc-related magmas and the initial concentration of Au, Ag and Cu. J. Petrol. 51, 2445–2464.

Jugo, P.J., Luth, R.W., Richards, J.P., 2005. Experimental data on the speciation of sulfur as a function of oxygen fugacity in basaltic melts. Geochim. Cosmochim. Acta 69, 497–503.

Jugo, P.J., Wilke, M., Botcharnikov, R.E., 2010. Sulfur K-edge XANES analysis of natural and synthetic basaltic glasses: implications for S speciation and S content as function of oxygen fugacity. Geochim. Cosmochim. Acta 74, 5926–5938.

Kelley, K.A., Cottrell, E., 2009. Water and the oxidation state of subduction zone magmas. Science 325, 605–607.

Kiseeva, E.S., Wood, B.J., 2013. A simple model for chalcophile element partitioning between sulphide and silicate liquids with geochemical applications. Earth Planet. Sci. Lett. 383, 68–81.

Kiseeva, E.S., Wood, B.J., 2015. The effects of composition and temperature on chalcophile and lithophile element partitioning into magmatic sulphides. Earth Planet. Sci. Lett. 424, 280–294.

Lee, C.T., Leeman, W.P., Canil, D., Li, Z., 2005. Similar V/Sc systematics in MORB and arc basalts: implications for the oxygen fugacities of their mantle source regions. J. Petrol. 46, 2313–2336.

Lee, C.T., Luffi, P., Chin, E.J., Bouchet, R., Dasgupta, R., Morton, D.M., Le Roux, V., Yin, Q.Z., Jin, D., 2012. Copper systematics in arc magmas and implications for crust-mantle differentiation. Science 336, 64–68.

Lee, C.T., Luffi, P., Le Roux, V., Dasgupta, R., Albarede, F., Leeman, W.P., 2010. The redox state of arc mantle using Zn/Fe systematics. Nature 468, 681–685.
Li, Y., 2014. Comparative geochemistry of rhenium in oxidized arc magmas and MORB and rhenium partitioning during magmatic differentiation. Chem. Geol. 386, 101–114.
Li, Y., Audétat, A., 2012. Partitioning of V, Mn, Co, Ni, Cu, Zn, As, Mo, Ag, Sn, Sb, W, Au, Pb, and Bi between sulfide phases and hydrous basanite melt at upper mantle conditions. Earth Planet. Sci. Lett. 355, 327–340.
Li, Y., Audétat, A., 2013. Gold solubility and partitioning between sulfide liquid, monosulfide solid solution and hydrous mantle melts: implications for the formation of Au-rich magmas and crust–mantle differentiation. Geochim. Cosmochim. Acta 118, 247–262.
Li, Y., Audétat, A., 2015. Effects of temperature, silicate melt composition, and oxygen fugacity on the partitioning of V, Mn, Co, Ni, Cu, Zn, As, Mo, Ag, Sn, Sb, W, Au, Pb, and Bi between sulfide phases and silicate melt. Geochim. Cosmochim. Acta 162, 25–45.
Lyons, T.W., Reinhard, C.T., Planavsky, N.J., 2014. The rise of oxygen in Earth's early ocean and atmosphere. Nature 506, 307–315.
Martin, H., Moyen, J.-F., 2002. Secular changes in tonalite-trondhjemite-granodiorite composition as markers of the progressive cooling of Earth. Geology 30, 319–322.
Mengason, M.J., Piccoli, P.M., Candela, P., 2010. An evaluation of the effect of copper on the estimation of sulfur fugacity (fS2) from pyrrhotite composition. Econ. Geol. 105, 1163–1169.
Metrich, N., Clocchiatti, R., 1996. Sulfur abundance and its speciation in oxidized alkaline melts. Geochim. Cosmochim. Acta 60, 4151–4160.
Moussallam, Y., Edmonds, M., Scaillet, B., Peters, N., Gennaro, E., Sides, I., Oppenheimer, C., 2016. The impact of degassing on the oxidation state of basaltic magmas: a case study of Kīlauea volcano. Earth Planet. Sci. Lett. 450, 317–325.
Müller, D., Groves, D., 2016. Potassic Igneous Rocks and Associated Gold-Copper Mineralization, fourth edition. Springer, pp. 1–297.
Mungall, J.E., 2002. Roasting the mantle: slab melting and the genesis of major Au and Au-rich Cu deposits. Geology 30, 915.
Muntean, J.L., Cline, J.S., Simon, A.C., Longo, A.A., 2011. Magmatic–hydrothermal origin of Nevada's Carlin-type gold deposits. Nat. Geosci. 4, 122–127.
Parat, F., Holtz, F., Streck, M.J., 2011. Sulfur-bearing magmatic accessory minerals. Rev. Mineral. Geochem. 73, 285–314.
Prouteau, G., Scaillet, B., 2012. Experimental constraints on sulphur behaviour in subduction zones: implications for TTG and adakite production and the global sulphur cycle since the Archean. J. Petrol. 54, 183–213.
Rowe, M.C., Kent, A.J.R., Nielsen, R.L., 2007. Determination of sulfur speciation and oxidation state of olivine hosted melt inclusions. Chem. Geol. 236, 303–322.
Rowe, M.C., Kent, A.J.R., Nielsen, R.L., 2009. Subduction influence on oxygen fugacity and trace and volatile elements in basalts across the cascade volcanic arc. J. Petrol. 50, 61–91.
Rudnick, R.L., Gao, S., 2014. Composition of the continental crust. Treatise Geochem. 4, 1–51.
Sillitoe, R., 1997. Characteristics and controls of the largest porphyry copper-gold and epithermal gold deposits in the circum-Pacific region. Aust. J. Earth Sci. 44, 373–388.
Sillitoe, R.H., 2002. Some metallogenic features of gold and copper deposits related to alkaline rocks and consequences for exploration. Miner. Depos. 37, 4–13.
Smythe, D.J., Wood, B.J., Kiseeva, E.S., 2017. The S content of silicate melts at sulfide saturation: new experiments and a model incorporating the effects of sulfide composition. Am. Mineral. 102, 795–803.
Spencer, C.J., Cavosie, A.J., Raub, T.D., Rollinson, H., Jeon, H., Searle, M.P., Miller, J.A., McDonald, B.J., Evans, N.J., 2017. Evidence for melting mud in Earth's mantle from extreme oxygen isotope signatures in zircon. Geology 45, 975–978.
Stagno, V., Ojwang, D.O., McCammon, C.A., Frost, D.J., 2013. The oxidation state of the mantle and the extraction of carbon from Earth/'s interior. Nature 493, 84–88.
Sun, W., Arculus, R.J., Kamenetsky, V.S., Binns, R.A., 2004. Release of gold-bearing fluids in convergent margin magmas prompted by magnetite crystallization. Nature 431, 975–978.
Tassara, S., Gonzalez-Jimenez, J.M., Reich, M., Schilling, M.E., Morata, D., Begg, G., Saunders, E., Griffin, W.L., O'Reilly, S.Y., Gregoire, M., Barra, F., Corgne, A., 2017. Plume-subduction interaction forms large auriferous provinces. Nat. Commun. 8, 843.
Toulmin, P., Barton, P.B., 1964. A thermodynamic study of pyrite and pyrrhotite. Geochim. Cosmochim. Acta 28, 641–671.
Wallace, P.J., 2005. Volatiles in subduction zone magmas: concentrations and fluxes based on melt inclusion and volcanic gas data. J. Volcanol. Geotherm. Res. 140, 217–240.
Wallace, P.J., Carmichael, I.S.E., 1994. S speciation in submarine basaltic glasses as determined by measurements of SKa X-ray wavelength shifts. Am. Mineral. 79, 161–167.
Wallace, P.J., Edmonds, M., 2011. The sulfur budget in magmas: evidence from melt inclusions, submarine glasses, and volcanic gas emissions. Rev. Mineral. Geochem. 73, 215–246.
Wang, Z., Becker, H., Liu, Y., Hoffmann, E., Chen, C., Zou, Z., Li, Y., 2018. Constant Cu/Ag in upper mantle and oceanic crust: implications for the role of cumulates during the formation of continental crust. Earth Planet. Sci. Lett. 493, 25–35.
Wilke, M., Klimm, K., Kohn, S.C., 2011. Spectroscopic studies on sulfur speciation in synthetic and natural glasses. Rev. Mineral. Geochem. 73, 41–78.
Zajacz, Z., Candela, P.A., Piccoli, P.M., Sanchez-Valle, C., Wälle, M., 2013. Solubility and partitioning behavior of Au, Cu, Ag and reduced S in magmas. Geochim. Cosmochim. Acta 112, 288–304.
Zajacz, Z., Candela, P.A., Piccoli, P.M., Wälle, M., Sanchez-Valle, C., 2012. Gold and copper in volatile saturated mafic to intermediate magmas: solubilities, partitioning, and implications for ore deposit formation. Geochim. Cosmochim. Acta 91, 140–159.
Zajacz, Z., Seo, J.H., Candela, P.A., Piccoli, P.M., Heinrich, C.A., Guillong, M., 2010. Alkali metals control the release of gold from volatile-rich magmas. Earth Planet. Sci. Lett. 297, 50–56.
Zhang, Z.-M., Shen, K., Sun, W.-D., Liu, Y.-S., Liou, J.G., Shi, C., Wang, J.-L., 2008. Fluids in deeply subducted continental crust: petrology, mineral chemistry and fluid inclusion of UHP metamorphic veins from the Sulu orogen, eastern China. Geochim. Cosmochim. Acta 72, 3200–3228.